

Anomalous Response of Floating Offshore Wind Turbine to Wind and Waves II: Adaptive Importance Sampling

Yihan Liu ^(1,2) and Michael (Misha) Chertkov ⁽¹⁾

⁽¹⁾ Program in Applied Mathematics & Department of Mathematics, University of Arizona, Tucson, AZ 85721, USA

⁽²⁾ Virginia Tech, Blacksburg, VA 24061, USA

Correspondence to chertkov@arizona.edu

December 5, 2024

Abstract

In this paper, we continue the reliability study initiated in [1] on the extreme values of key mechanical characteristics – pitch, surge, and heave – of a floating offshore wind turbine (FOWT). Utilizing a comprehensive list of wind and wave patterns that cause anomalously large deviations in FOWT characteristics, originally revealed via brute-force Markov Chain Monte Carlo (MCMC) simulations, we have developed an efficient Adaptive Importance Sampling (AIS) MCMC. This new approach enables us to bootstrap and uncover the tails of the probability distributions associated with even higher and potentially more damaging values of pitch, surge, and heave which are not accessible through standard MCMC. Enhanced modeling of fluctuations in the large-scale wind component has allowed us to identify and examine both previously known and new rare but dangerous regimes. Notably, using AIS-MCMC, we pinpoint and analyze a surge anomaly driven by rare coherent wind patterns with relatively low mean values and wave interactions that interfere with wind turbine control.

1 Introduction

With a growing global focus on protecting the environment, renewable energy sources have become essential. Leading the way, wind power has emerged as the United States’ largest renewable energy source, preventing 334 million metric tons of **CO₂** emissions in 2022 [2]. Floating offshore wind turbines (FOWTs) have gained traction, especially in deep-water locations over 60 meters. These systems bring several advantages over onshore and fixed-bottom offshore turbines. By accessing higher wind speeds in open marine environments, FOWTs boost power generation capacity. Additionally, they minimize visual and noise impacts, lower costs, and reduce land use. The wider deployment of FOWTs highlights the urgent need for turbines that are both reliable and high-performing. Yet, these structures face continuous exposure to unpredictable wind and wave forces, leading to mechanical stresses that affect various turbine components.

Studying these extreme events is crucial for several reasons. First, the safety and structural integrity of FOWTs depends on understanding and mitigating risks posed by rare but severe conditions, such as storms and rogue waves. Designing platforms that can withstand these extremes is essential to prevent catastrophic failures. Second, reliability is key to ensuring a consistent and uninterrupted supply of renewable energy. By analyzing the impact of rare events, engineers can predict and reduce the likelihood of performance issues or failures, thereby minimizing downtime and maintenance costs. Finally, understanding rare events is vital for effective risk management and insurance planning. Accurate assessments of extreme conditions help insurers set appropriate premiums and allow operators to develop risk mitigation strategies, ultimately reducing financial uncertainty. In light of these considerations, this study aims to develop an efficient methodology for generating and analyzing rare events in FOWT operations.

One general approach to studying rare events is through Markov-Chain Monte Carlo (MCMC) simulation, which involves a large number of simulations with stochastic wind and wave inputs. A brute-force MCMC analysis of rare events for FOWTs was explored in [1], providing an initial analysis of how environmental conditions impact turbine operations. However, MCMC methods can be highly inefficient

in practice when applied to rare event sampling. Because rare events occur with such low probability, a significant portion of the MCMC samples will capture typical, and only a tiny fraction of the simulations contribute useful information about rare events, resulting in a considerable waste of computational resources.

The inefficiency of brute-force MCMC methods presents a major limitation for rare event studies. A targeted approach focused on the most relevant extreme events would reduce computational costs. To address these limitations, this study introduces an adaptive importance sampling approach and experiments on its performance applied to FOWT. Unlike brute-force MCMC, importance sampling biases the sampling process towards the regions of interest—specifically, the rare and extreme events that are critical for FOWT reliability analysis. By focusing computational effort on these low-probability, high-impact events, importance sampling significantly increases the likelihood of capturing useful information about rare events while reducing the overall number of simulations required. Additionally, adaptive importance sampling can be refined iteratively to improve the sampling distribution based on observed data, further enhancing its efficiency in capturing rare events. Through this approach, we aim to establish a more practical and cost-effective methodology for studying rare events in offshore wind turbine operations.

In this paper, we build upon the study initiated in [1], which utilized Betti’s model [3] to analyze rare events in floating offshore wind turbine operations. Our focus remains on the NREL 5MW wind turbine [4] and the Tension-Leg Platform (TLP) design [5] shown in Figure 1. In this work, we extend the previous study by enhancing the wind and wave models, as well as refining the baseline control system which is presented in the following section.

The paper is structured as follows: Section 2 details the general model framework, including the stochastic wind and wave representations and the baseline control system in addition to [1]. Section 3 provides a general importance sampling (IS) formulation and simulation results. Section 4 outlines the non-parametric adaptive IS methodology, illustrating the iterative approach used to refine the sampling distribution for rare events and interpretations in different features. Finally, Section 5 concludes with an evaluation of the AIS method’s effectiveness, discussing its potential implications for the design and reliability assessment of offshore wind systems and future research directions.

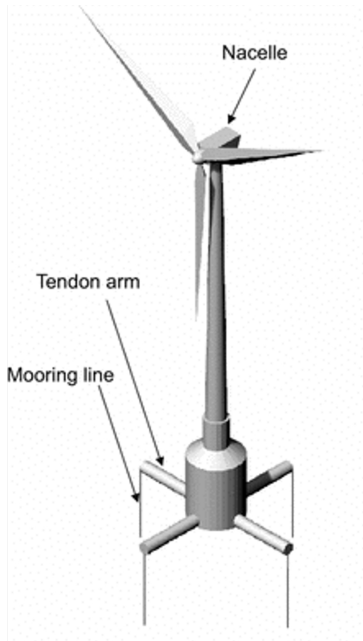


Figure 1: Tension Leg Platform (TLP) design. Taken from [6]

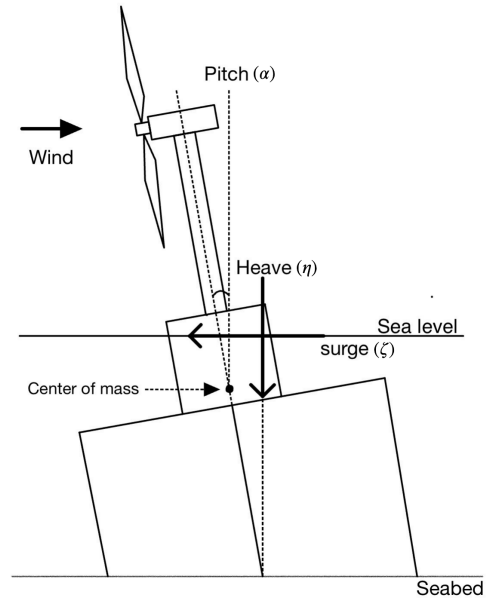


Figure 2: The 2-dimension representation of TLP-based FOWT in the Betti model.

2 Model & Controller Implementation

In this paper, we continue to use the modeling framework developed in our previous study [1], which focuses on the TLP design shown in Figure 1 and adapted from the Betti’s model [3]. This model captures

the essential dynamics of a floating offshore wind turbine (FOWT) by focusing on two main components: the platform (non-rotating part) and the drivetrain (rotating part). For clarity and self-containment, we provide an overview of the model's key aspects here, while directing readers to our earlier work Section 5 in [1] for a detailed description.

The FOWT platform model is simplified in two dimensions shown in Figure 2 to achieve a balance between computational efficiency and the ability to capture key dynamic behaviors under extreme environmental conditions. We consider three Degrees of Freedom (DOF): surge, heave, and pitch (ζ, η, α), and associated derivatives (velocities) of each DOF (v_ζ, v_η, ω). Combined with the drivetrain dynamics that account for the rotor speed ω_R , result in 7 components in the state vector:

$$\mathbf{x} = [\zeta \ v_\zeta \ \eta \ v_\eta \ \alpha \ \omega \ \omega_R]^T \quad (1)$$

Derived the dynamic system with stochastic input ξ :

$$t \in [0, T] : \quad \dot{\mathbf{x}}(t) = \mathbf{f}(\mathbf{x}(t), \xi), \quad (2)$$

$$\mathbf{x}_0 = \mathbf{x}(0) \sim p_0, \quad \xi \sim p_{\text{ex}}, \quad (3)$$

where T represents a preset time interval (such as 10 minutes, 20 minutes, or 1 hour). The system is initialized with $\mathbf{x}(0)$ drawn from an exogenously given probability distribution $p_0(\cdot)$. Additionally, ξ is a finite-dimensional vector of time-independent stochastic parameters that characterize wind and wave signals (for instance, representing leading harmonics in the Fourier-frequency representation) drawn from the probability distribution $p_{\text{ex}}(\cdot)$.

In our previous work [1], we conducted an initial Markov Chain Monte Carlo (MCMC) simulation to capture rare events under high wind conditions, focusing specifically on speeds above the rated. In this paper, we expand our study to cover the full operational range of the NREL 5MW turbine, which includes performance at lower wind speeds, rated conditions, and transitions between different control regions. To support this broader scope, we have enhanced our wind generation process and expanded the implementation of the baseline control system.

2.1 Environment's Model

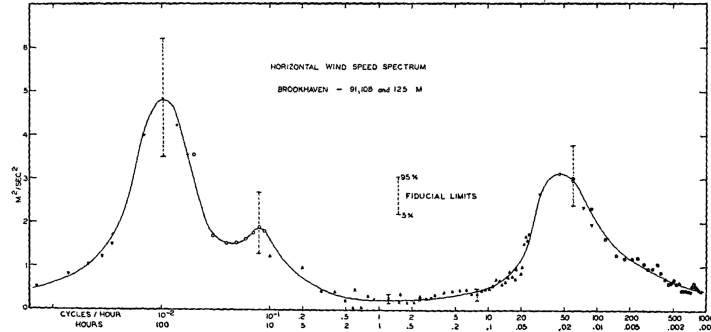


Figure 3: Van der Hoven's spectral model, taken from [7]

Our wind model covers all operation regions of the wind turbine. The wind speed ranges from less than 5 m/s to more than 30 m/s. This is achieved by following the procedure given in [8]. This stochastic wind model considers two frequency domains: low and high.

The low-frequency domain of large-scale components covers the domain from 0.001 to 3 cycles per hour. We utilized Van der Hoven's spectral model [7] to simulate large-scale turbulence components. Figure 3 shows the power intensity at different frequencies. Note that this power spectral does not depend on the average wind speed. We consider discrete angular frequencies $\omega_i, i = 1, 2, \dots, N_{lo} + 1$ in the low-frequency domain and compute the amplitude in each frequency ω_i as follows:

$$A_i = \frac{2}{\pi} \sqrt{\frac{1}{2} [S_{VH}(\omega_i) + S_{VH}(\omega_{i+1})] \cdot [\omega_{i+1} - \omega_i]} \quad (4)$$

where S_{VH} represents Van der Hoven's spectral intensity. To get the time domain large-scale velocity component, we calculate a cosine series:

$$v_{lo}(t) = v_{bar} + \sum_{i=1}^{N_{lo}} A_i \cos(\omega_i t + \varphi_i) \quad (5)$$

-where v_{bar} is the average wind speed. φ_i is a random phase corresponding to the frequency i . This random phase is generated using uniform distribution between $-\pi$ to π . Define the finite vector ξ_{lo} of random phase to generate large-scale wind components as follows:

$$\xi_{lo} = [\varphi_1, \varphi_2, \varphi_3, \dots, \varphi_{N_{lo}}] \quad (6)$$

This long-scale wind component has a step size T_l in the scale of minutes, we set $T_l = 180$ seconds.

The high-frequency domain of short-scale components covers the range from 4 to 1000 cycles per hour. We use the Von Karman's power spectrum:

$$S_{VK}(\omega) = \frac{0.475\sigma^2 \frac{L}{\bar{v}}}{[1 + (\frac{\omega L}{\bar{v}})^2]^{5/6}} \quad (7)$$

Where σ is the turbulence intensity and L is the turbulence length scale, \bar{v} is the average wind speed. We set $L = 180m$ as a starting point. To generate the short-scale wind velocity in the time domain, we apply the shaping filter to the power spectral and compute the impulse response of the filter, calling it $h(t)$, then take the convolution of the impulse response and a white noise input utilized in Eq. (8)

$$v_{sh}(t) = \int_0^t h(\tau) w(t - \tau) d\tau \quad (8)$$

Misha says: May be you should also introduce N_{sh} phases of short scale harmonics which becomes the components of ξ_{sh} .

Where $v_{sh}(t)$ is the short-scale wind speed in the time domain, $w(t)$ is the white noise, a normal distribution around 0 with unity variance. The time step to update short-scale wind components is $T_s = 1$ second.

Algorithm 2.1 provides the wind generation process. Refer to section III in [8] for detailed wind generation steps, parameters, and numerical solutions.

Algorithm 1 Generate wind

- 1: Set average wind speed v_{bar} , T_l , T_s , and total simulation duration T
 - 2: Generate large-scale wind components using Van der Hoven's spectral and Eq. (5) for a total time T with step size T_l . Call the generated long-scale wind speed list \mathbf{v}_{long}
 - 3: **for** each v_{longi} in \mathbf{v}_{long} **do**
 - 4: Update parameters, set \bar{v} in Eq. (7) to v_{longi} and update turbulence intensity parameter σ
 - 5: Compute the impulse response of Eq. (7) by applying a shaping filter
 - 6: Generate a white noise, then generate the small-scale wind component for the duration of T_l by computing the convolution of the impulse response and the white noise
 - 7: **end for**
-

The waves are generated according to the Pierson–Moskowitz spectrum [9]. The Pierson–Moskowitz spectral density $S_{PM}(f)$ is given by:

$$S_{PM}(f) = \frac{\alpha_{PM} g^2}{(2\pi)^4 f^5} \exp\left(-\frac{5}{4} \left(\frac{f}{f_{PM}}\right)^{-4}\right) \quad (9)$$

where $\alpha_{PM} = 0.0081$, g is gravitational acceleration, and f_{PM} is the peak frequency, determined by the mean wind speed. To generate a random wave realization, the frequency range is divided into bands of width Δf , with each band's amplitude a_i , $i = 1, 2, \dots, N_{wa}$ is determined by $a_i = \sqrt{2S_{PM}(f_i)\Delta f}$. The surface elevation at any point x and time t is then computed as:

$$\eta_{wa}(x, t) = \sum_{i=1}^{N_{wa}} a_i \sin(2\pi f_i t - k_i x + \phi_i) \quad (10)$$

where ϕ_i is a random phase angle, uniformly distributed in $[0, 2\pi)$, and k_i is the wave number for each frequency f_i , assuming deep water conditions.

Misha says: May be you should also introduce N_{wa} phases wave harmonics which becomes the components of ξ_{wa} .

As the increased range of wind speed fluctuation, the strength of the waves also changes with wind speed. We use the long-scale wind speed as the wind speed parameter for wave generation linked to the peak frequency f_{PM} . Figure 4 is an example of generated wind and wave signals. The red line in the wind speed plot represents the large-scale component. Notably higher wind speeds have stronger turbulence intensity and higher waves.

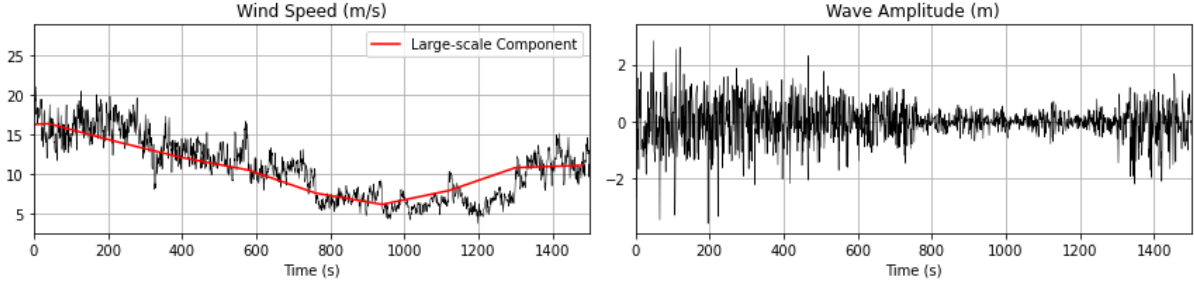


Figure 4: Example of generated wind and wave signal with global average wind speed at 11 m/s.

2.2 Baseline Control System Implementation

We implemented the Baseline Control System used in the NREL offshore 5-MW wind turbine described in [4] which features both generator-torque and blade-pitch controllers. This system enables the turbine to operate effectively across a broader range of environmental conditions. In this section, we provide an overview of the control design and assess its performance in our simulation environment.

The control system divides turbine operation into specific regions based on the generator (rotor) speed. The rated rotor speed is 12.1 rpm, and the rated wind speed is 11.4 m/s. When the generator speed is below or equal to the rated (Region 2), the primary goal is to maximize power production. In this region, generator-torque controller is used to maintain an optimal tip-speed ratio, and the blade pitch angle is fixed at 0° .

As wind speeds reach or exceed the rated threshold (Regions 2.5 and 3), the focus of control shifts to limiting the mechanical loads on the system. Here, both the generator torque controller and the blade-pitch controller are activated to regulate the generator speed and maintain a constant power output.

2.2.1 Control-Measurement Filter

To prevent high-frequency noise from affecting the control systems, we implemented a recursive, single-pole low-pass filter with exponential smoothing on rotor (generator) speed as the input for both the generator-torque and blade-pitch controllers, filtered using the following discrete-time recursion equation:

$$y[n] = (1 - \alpha(n))u[n] + \alpha y[n - 1] \quad (11)$$

where $y[n]$ is the filtered generator speed, $u[n]$ is the unfiltered speed, and α is the filter coefficient determined by the corner frequency. The filter was designed with a corner frequency of 0.25 Hz, approximately one-quarter of the blade's first edgewise natural frequency.

2.2.2 Generator Torque Controller

The generator-torque controller operates based on the filtered generator speed and follows a region-based control law typical for wind turbines. It incorporates five control regions. In Region 1, the turbine does not extract power, allowing the rotor to accelerate. Region $1\frac{1}{2}$ serves as a transitional phase, ensuring a minimum generator speed as it shifts into Region 2. In Region 2, the turbine maximizing power production, with the blade pitch angle fixed at 0° and generator torque set proportional to the square of the generator speed. Region $2\frac{1}{2}$ transitions toward Region 3, where the controller limits tip speed to prevent excessive rotor velocities. Finally, in Region 3, the turbine operates in constant power mode:

generator torque becomes inversely proportional to generator speed, and the blade pitch angle controller is activated to maintain a stable rotor speed.

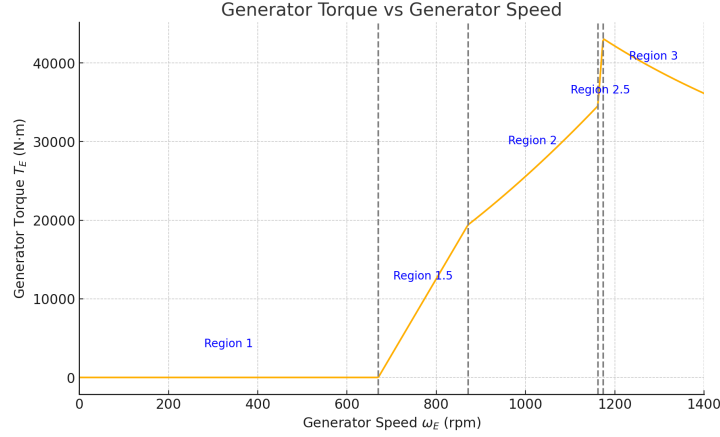


Figure 5: Generator torque versus generator speed at different control regions.

Figure 5 illustrates the generator torque across each control region. The peak power coefficient was determined to be 0.482 at a tip-speed ratio of 7.55, which resulted in an optimal proportionality constant of 0.0255764 N·m/rpm² for Region 2. The generator torque for a given generator speed ω_E (rpm) in all regions is derived by the following piecewise equations:

$$T_E(\omega_E) = \begin{cases} 0, & \text{if } \omega_E < 670 \text{ rpm (Region 1)} \\ 96.53386 \cdot \omega_E - 64,677.68667, & \text{if } 670 \leq \omega_E < 871 \text{ rpm (Region 1.5)} \\ 0.0255764 \cdot \omega_E^2, & \text{if } 871 \leq \omega_E < 1,161.963 \text{ rpm (Region 2)} \\ 729.4343 \cdot \omega_E - 813,043.45, & \text{if } 1,161.963 \leq \omega_E < 1,173.7 \text{ rpm (Region 2.5)} \\ \frac{158,898,300}{\pi \omega_E}, & \text{if } \omega_E \geq 1,173.7 \text{ rpm (Region 3)} \end{cases} \quad (12)$$

The torque limit was set to 10% above the rated torque to avoid excessive overload, while the torque rate was limited to 15,000 N·m/s.

2.2.3 Blade Pitch PI-Controller

In Region 3, where the turbine operates at constant power, the blade-pitch controller regulates generator speed through a proportional-integral (PI) control system that responds to the difference between the filtered generator speed and the rated generator speed. This control design is based on a single-degree-of-freedom (DOF) model of the wind turbine shaft rotation, which provides the basis for computing the required PI gains.

The PI controller was designed to achieve a natural frequency of $\omega_{\phi n} = 0.6$ rad/s and a damping ratio ζ_ϕ between 0.6 and 0.7. These values were chosen to provide adequate stability while minimizing overshoot. To adapt to variations in aerodynamic power sensitivity to the blade-pitch angle across Region 3, we implemented gain scheduling based on the blade-pitch angle, allowing the proportional and integral gains to adjust dynamically.

The relationship between the pitch angle perturbations and rotor-speed error is given by the following control law:

$$\Delta\theta = K_P N_{\text{Gear}} \Delta\Omega + K_I N_{\text{Gear}} \int \Delta\Omega dt + K_D N_{\text{Gear}} \frac{d(\Delta\Omega)}{dt} \quad (13)$$

where $\Delta\theta$ is the pitch angle adjustment. $\Delta\Omega$ is the speed error. N_{Gear} is the gearbox ratio. K_P , K_I , and K_D are the proportional, integral, and derivative gains, respectively.

For this controller, we used only the proportional and integral terms, neglecting the derivative term to avoid additional complexity and potential instability. This yields the simplified PI control law:

$$\Delta\theta = K_P N_{\text{Gear}} \Delta\Omega + K_I N_{\text{Gear}} \int \Delta\Omega dt \quad (14)$$

The gains were computed based on the desired response characteristics. Using the sensitivity of aerodynamic power to blade-pitch angle, $\frac{\partial P}{\partial \theta}$, the proportional and integral gains are given by:

$$K_P = \frac{2I_{\text{Drivetrain}} \Omega_0 \zeta \phi \omega_{\phi n}}{N_{\text{Gear}} \left(\frac{\partial P}{\partial \theta} \right)} \quad (15)$$

$$K_I = \frac{I_{\text{Drivetrain}} \Omega_0 \omega_{\phi n}^2}{N_{\text{Gear}} \left(\frac{\partial P}{\partial \theta} \right)} \quad (16)$$

where $I_{\text{Drivetrain}}$ is the drivetrain inertia, Ω_0 is the rated low-speed shaft rotational speed.

A gain-correction factor is applied to both K_P and K_I to account for the near-linear variation of pitch sensitivity with blade-pitch angle. This gain-scheduling approach ensures the controller remains responsive to speed fluctuations while maintaining stability across Region 3. Additionally, we set the blade-pitch rate limit to $8^\circ/\text{s}$ and confined the blade-pitch angle within 0° (for maximum power in Region 2) to 90° (for fully feathered, neutral torque).

2.2.4 Control Performance in Simulation

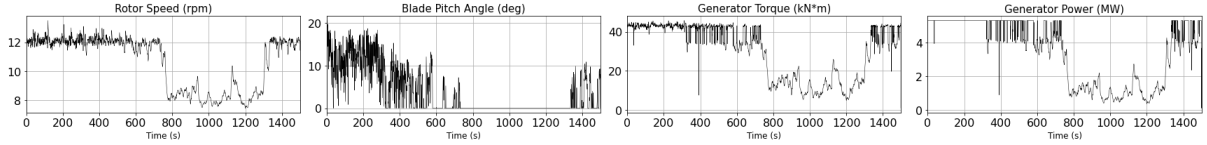


Figure 6: Drivetrain properties with the baseline control system subjected to the wind and wave signals depicted in Figure 4.

Figure 6 shows the simulation output with the baseline control system implemented response to the wind and wave signals shown in Figure 4. The output plots display key turbine variables, including rotor speed, blade pitch angle, generator torque, and generator power.

When the wind speed exceeds the rated value of 11.4 m/s, the controller effectively regulates the rotor speed around the rated 12.1 rpm, as shown by the relatively stable rotor speed plot, and maintains a constant power strategy. During these periods, the blade pitch controller becomes active, adjusting the blade pitch angle to control the aerodynamic load on the rotor.

When the wind speed is below the rated value, the blade pitch angle remains inactive, fixed around 0° to maximize power capture. During these periods, the generator-torque controller operates to maximize the power output by adjusting the generator torque, as illustrated by the generator torque and power plots.

Overall, the simulation results demonstrate that the control system successfully regulates rotor speed and power output across different wind conditions. The transition between regions is also smooth. The pitch controller engages when wind speeds exceed rated, providing stability, while the generator-torque controller efficiently maximizes power capture when wind speeds are below rated.

3 Empirical Importance Sampling

Consider a general equation governing the dynamics of the system's state vector in Eq. (2). To study the dynamics of a single wind turbine under stochastic wind and wave influences, we focus on its mechanical and rotational features, denoted by \mathbf{x} , include pitch, heave, surge, and their time derivatives, and rotor speed. The equation governing \mathbf{x} describes how these features interact with harmonics in the environmental forcing, represented by $\boldsymbol{\xi}$, which encapsulates stochastic variations in wind and wave conditions.

Here we limit our analysis to the dynamics of a single turbine. While the framework can extend to more complex systems, such as a full wind farm with electrical features and inter-turbine dynamics.

As we will see below, we detail the exogenous stochastic vector, ξ , by splitting it into three components: $\xi = (\xi_{\text{wind-long}} = \xi_{\text{lo}}, \xi_{\text{wind-short}} = \xi_{\text{sh}}, \xi_{\text{waves}} = \xi_{\text{wa}})$. This split is significant as it determines the factorization of the joint probability distribution function of these components:

$$p_{\text{ex}}(\xi) = p_{\text{sh}|\text{lo}}(\xi_{\text{sh}}|\xi_{\text{lo}})p_{\text{wa}|\text{lo}}(\xi_{\text{wa}}|\xi_{\text{lo}})p_{\text{lo}}(\xi_{\text{lo}}), \quad (17)$$

which indicates the causal dependencies among the three components: the large-scale wind parameterized by ξ_{lo} is independent of the other components, while the small-scale wind parameterized by ξ_{sh} and the waves parameterized by ξ_{wa} are independent of each other but both are conditioned on the large-scale wind.

We are interested in computing/estimating

$$R = \mathbb{E}_{\text{Eqs. (2,3)}} \left[\chi(\cdot) \middle| \text{Eq. (1)} \right]. \quad (18)$$

Here in Eq. (18), $\chi(\cdot)$ is a characteristic function of extreme/rare events (equal to unity if the condition in its argument is satisfied and zero otherwise). We focus on estimating Eq. (18) by highlighting the significance of the rare event estimation, and therefore the typical values (of $\mathbf{x}(0)$ and ξ) contribute exactly zero to Eq. (18).

The importance sampling approach to estimating R defined in Eq. (18) consists in rewriting it as

$$R = \mathbb{E}_{\mathbf{x}_0, \xi \sim q} \left[\frac{\chi(\cdot) p_{\text{ex}}(\xi)}{q(\xi)} \middle| \text{Eq. (1)} \right], \quad (19)$$

where $q(\cdot, \cdot)$ is a probe probability distribution adjusted to yield an $O(1)$ contribution for the typical values of the expressions under the expectation in Eq. (19).

A practical difficulty in utilizing importance sampling to compute R is discovering an appropriate $q(\cdot, \cdot)$. An empirical approach to resolving this problem involves using direct MCMC, which does not account for the condition in the argument of the χ -function in Eq. (19), to discover events that satisfy the condition. Suppose that Ξ such events are discovered:

$$s = 1, \dots, \Xi: \quad \{\mathbf{x}^{(s)}(t)\}, \xi^{(s)}, \quad \text{s.t. } \forall t \quad \dot{\mathbf{x}}^{(s)} = \mathbf{f}(\mathbf{x}^{(s)}, \xi^{(s)}), \quad \chi(\cdot) = 1. \quad (20)$$

We can then use this brute force data to form a ϵ -regularized empirical probe function:

$$q(\mathbf{x}_0, \xi) = \frac{1}{\Xi} \sum_{s=1}^{\Xi} \prod_i \mathcal{N}(x_{i;0} | x_{i;0}^{(s)}; (\epsilon x_{i;0}^{(s)})^2) \prod_{\alpha} \mathcal{N}(\xi_{\alpha} | \xi_{\alpha}^{(s)}; (\epsilon \xi_{\alpha}^{(s)})^2), \quad (21)$$

where ϵ is sufficiently small.

The empirical selection of the probability distribution can also serve as a starting point for an adaptive search for the best (or simply good) probe distribution, thus prompting adaptive importance sampling approaches. See [10] for a review and [11] for a recent implementation.

3.1 Formulation with Empirical Extreme Events

Starting IS with empirical extreme events, a new set of standard MCMC simulations of 10,000 samples was conducted under the extended environment model and controllers, with a global average wind speed of 11 m/s. Each sample duration is set to 25 minutes, allowing sufficient time for significant variations in large-scale wind components to emerge, while still making it feasible to run a large number of configurations. Figure 7 shows the distribution of wind and wave signals. To prevent negative wind speeds, a lower bound of 1 m/s was manually applied to the large-scale component, accounting for the peak observed in the left tail of Figure 7

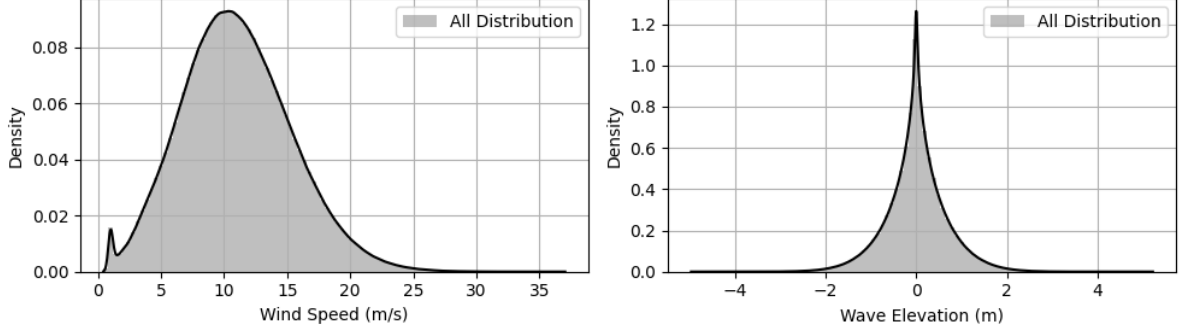


Figure 7: The PDF of wind and wave signals from 10,000 MCMC simulation.

The latest brute-force MCMC experiments evidence that the large-scale (long-time) components of wind play a crucial role in forming extreme phenomena of interest. We can leverage this and also the factorized way fluctuations of wind and waves enter the problem (see Eq. (17) to construct IS by biasing only the large-scale component of velocity. First, we sample the large-scale component of wind from the rare samples of interest received from the brute-force MCMC, and then we independently sample the small-scale component of wind and waves conditioned on the large-scale component of wind. In other words, we suggest making only the large-scale component of wind, ξ_{lo} , subject to IS, and then sampling ξ_{sh}, ξ_{wa} conditioned on ξ_{lo} according to the standard formula Eq. (17). This is formalized as follows:

$$q\left(\xi \middle| \{\xi_{lo}^{(s)}; s = 1, \dots, \Xi\}; \epsilon\right) = p_{sh|lo}(\xi_{sh}|\xi_{lo})p_{wa|lo}(\xi_{wa}|\xi_{lo}) \prod_{s=1}^{\Xi} \prod_{\alpha \in \Sigma_{lo}} \mathcal{N}\left(\xi_{\alpha;lo} \middle| \xi_{\alpha;lo}^{(s)}; (\epsilon \xi_{\alpha;lo}^{(s)})^2\right), \quad (22)$$

where Σ_{lo} is the set indexing harmonics of the large-scale (long-time) components of wind.

The starting point for our empirical importance sampling approach will be the exploration of the case where we pick only one sample discovered in the direct (brute force) MCMC, that is the case of Eq. (21) and Eq. (22) with $n = 1$. We will call it the reference sample. Then, guided by Eq. (22) we will extract $\xi_{lo}^{(1)}$ (and also $x_0^{(1)}$, which we will skip mentioning in the following for brevity) from the reference sample, and will focus on computing the following expectation conditioned on the reference value of $\xi_{lo}^{(1)}$:

$$R_{cond}\left(\xi_{lo}^{(1)}; \epsilon; S\right) = \mathbb{E}_{\xi \sim q\left(\cdot \middle| \xi_{lo}^{(1)}; \epsilon\right)} \left[\chi(\cdot) \middle| \text{Eq. (1)} \right] \quad (23)$$

$$\xrightarrow{\epsilon \rightarrow 0} \mathbb{E}_{\xi_{sh} \sim p_{sh|lo}(\cdot|\xi_{lo}^{(1)}); \xi_{wa} \sim p_{wa|lo}(\cdot|\xi_{lo}^{(1)})} \left[\chi(\cdot) \middle| \text{Eq. (1)} \right], \quad (24)$$

which should be viewed as a conditioned version of Eq. (19). We define the characteristic function $\chi(\cdot)$ for each type of anomaly or extreme event and will be provided in the following subsections for each event we considered.

Returning to the case with $\Xi > 1$ of multiple reference values we will study the following version of Eq. (19)

$$\begin{aligned} R\left(\{\xi_{lo}^{(s)}; s = 1, \dots, \Xi\}; \epsilon; S\right) &= \mathbb{E}_{\xi \sim q\left(\cdot \middle| \{\xi_{lo}^{(s)}; s=1, \dots, \Xi\}; \epsilon\right)} \left[\frac{\chi(\cdot) p_{ex}(\xi)}{q\left(\xi \middle| \{\xi_{lo}^{(n)}; n = 1, \dots, N\}; \epsilon\right)} \middle| \text{Eq. (1)} \right] \\ &= \mathbb{E}_{\xi \sim q\left(\cdot \middle| \{\xi_{lo}^{(s)}; s=1, \dots, \Xi\}; \epsilon\right)} \left[\chi(\cdot) \prod_i^{N_{lo}} \frac{U(\varphi_i|[0, 2\pi])}{\Xi^{-1} \sum_{s=1}^{\Xi} \mathcal{N}\left(\varphi_i|\varphi_i^{(s)}; \epsilon(\varphi_i^{(s)})^2\right)} \middle| \text{Eq. (1)} \right] \\ &= \mathbb{E}_{\xi \sim q\left(\cdot \middle| \{\xi_{lo}^{(s)}; s=1, \dots, \Xi\}; \epsilon\right)} \left[\chi(\cdot) \prod_i^{N_{lo}} \frac{\Xi}{2\pi \sum_{s=1}^{\Xi} \mathcal{N}\left(\varphi_i|\varphi_i^{(s)}; \epsilon(\varphi_i^{(s)})^2\right)} \middle| \text{Eq. (1)} \right] \end{aligned} \quad (25)$$

where $U(\cdot, [0, 2\pi])$ is the uniform distribution over $[0, 2\pi]$ for respective phase.

3.2 Reference Sample IS Implementation

In this section, we focus on sampling two types of anomaly/extreme events related to pitch and surge. In the following subsections, we detail an IS approach for these two types of events.

The first type of anomaly we are interested in sampling is based on the study conducted by [1], which investigates long-term pitch events. This study is particularly intriguing as it observed pitch instability lasting over extended periods (exceeding 8 minutes) without any apparent cause. To gain a deeper understanding of this anomaly, we will concentrate on sampling similar pitch events.

The second extreme event we study involves surge events as described in Section 4.4.4 of [5]. These extreme events are characterized by oscillations in surges that exceed the range of -1m to 8m , which is outside the main wave-energy spectrum.

3.2.1 Reference Sample for Long-Term Pitch Events

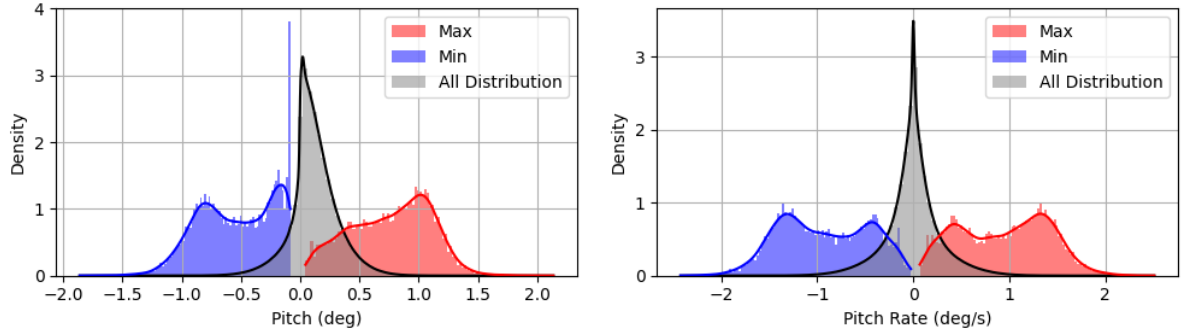


Figure 8: Pitch angle and pitch rate distribution

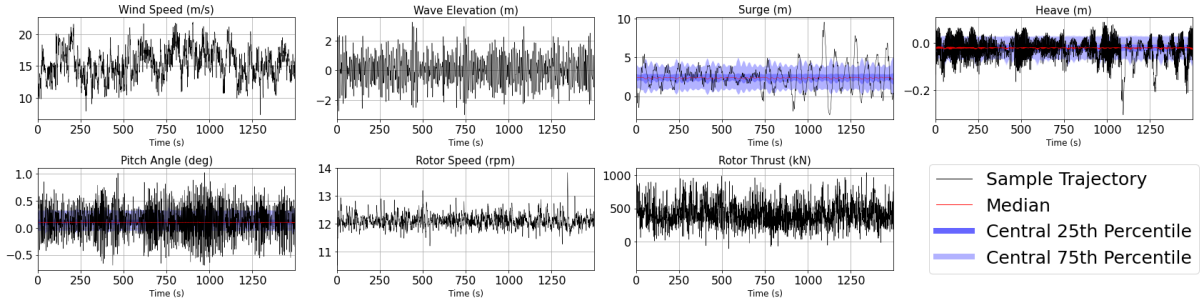


Figure 9: Threshold example, the long-term pitch anomaly

We start with the standard MCMC simulations. Figure 8 illustrates the probability density functions (PDFs) of the pitch angle and its derivative for 10,000 samples, each with a duration of 25 minutes. The figure also included the probability distribution of extreme values (max and min) observed in each sample. Since pitch instability lasts for a long period, standard deviation is a good indicator for this type of anomaly. The overall standard deviation of the pitch angle is 0.195° . We identified samples with significant pitch events by selecting those with large standard deviations. We define the characteristic function $\chi_\alpha(\cdot)$ as follow:

$$\chi_\alpha(\xi^\alpha, S) = \begin{cases} 0, & \text{std}_\alpha < S, \\ 1, & \text{std}_\alpha \geq S. \end{cases} \quad (26)$$

Note α is the state pitch in Eq. (1).

We begin by setting S to the top one percent of the standard deviation, which corresponds to a value of $S = 0.3259$. Such $\chi(\cdot, S)$ identifies the samples with the strongest pitch variations, where only the top 1% of the samples exhibit such unstable behavior. Figure 9 displays an example of this threshold of the

pitch state along with wind, wave signals, surge, heave, rotor speed, and rotor thrust. Percentile plots are color-coded for reference. Notably, similar long-term pitch events identified in [1] are also indicated.

From the analysis in [1], the long-term pitch anomaly can be identified with only the wind signal and without any waves (in still water). This suggests that wind plays a dominant role in causing these long-term events. Inspired by this finding, and following the formulation, we first identify an interesting wind signal through a brute-force approach and then establish an IS process based on the large-scale wind component ξ_{lo} of the selected sample(s).

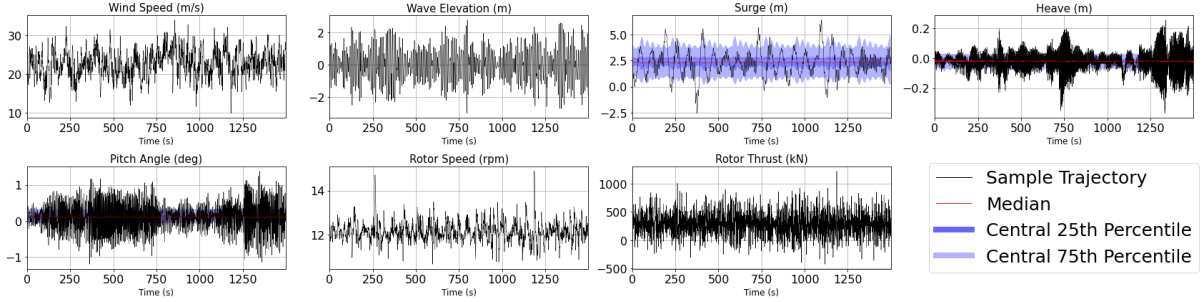


Figure 10: Selected sample with long-term anomaly as the start point of important sampling

Figure 10 shows our selection of the sample with long-term pitch anomaly from the brute force MCMC simulation. The percentile region is subject to the original MCMC output. We selected this sample because it has a strong pitch instability with a standard deviation of 0.398 which is beyond the threshold. Also, the fluctuation in other features (surge, heave) are relatively typical so we have a focus on pitch features. We extract the long-scale wind component from this sample and begin IS. We start with $\epsilon = 0$ in Eq. (21). In other words, we pick the ξ_{lo} to be exactly equal to the chosen sample. This first sampling stage increased the expectation of $\chi(S = 0.3259)$ from 0.01 to 0.07, and the overall standard deviation raised from 0.195 to 0.293. The results of the convergence test are given in Table 1. Based on the convergence test, we concluded that the sample size of 2,500 is sufficient at this stage.

Number of Samples	# of hits = events with $\chi(S = 0.3259) = 1$	R_{cond}
1,000	66	0.066
2,500	199	0.0796
5,000	369	0.0738
10,000	688	0.0688
15,000	1,103	0.0735
20,000	1,391	0.0696

Table 1: Importance sampling performance for different number of samples.

Figure 11 shows the probability density functions (PDFs) of the pitch angle from importance sampling compared with the original MCMC. The red region represents the distribution from importance sampling, while the gray region represents the traditional MCMC distribution. The plot uses the same legend as Figure 8 which includes the extreme value distribution observed in each sample. Notably, the overall distribution and extreme value distribution are more distinct, indicating a greater bias toward extreme values.

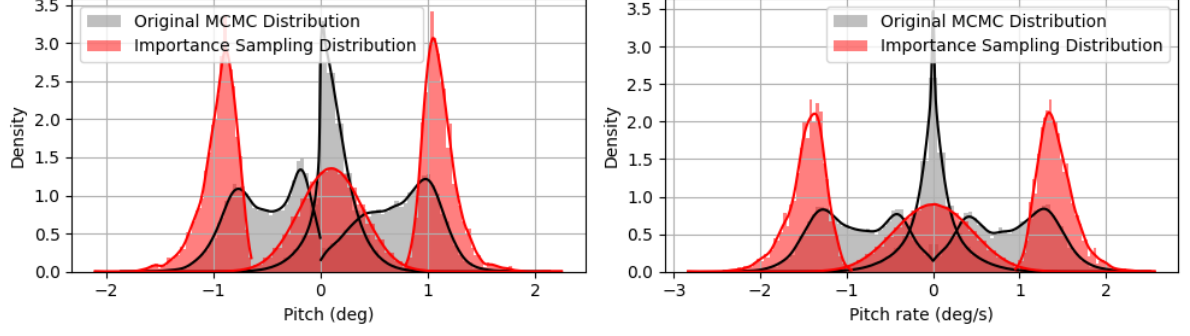


Figure 11: Probability distribution of pitch conditioned to $\xi_{lo}^{\alpha(1)}$ ($\epsilon = 0$) vs unconditioned.

We also compared conditionals, computed according to Eq. (23) with $\epsilon = 0$, for different anomalous pitch reference values of $\xi^{\alpha(1)}, \dots, \xi^{\alpha(N)}$, where the configurations are chosen for the N largest standard deviation. The sampling amount for each configuration is 2,500. Table 2 illustrates the IS performance R on 5 different reference configurations with $\epsilon = 0$. Figure 12 shows accumulated probability distribution results (averaging over all N cases together). Figure 13 shows how important sampling bias the wind signal for each reference configuration.

Configuration ID	# of hits = events with $\chi(S = 0.3259) = 1$	R_{cond}
1	199	0.0796
2	86	0.0344
3	186	0.0744
4	188	0.0752
5	222	0.0888

Table 2: Performance of importance sampling around different anomalous configurations (different IDs) extracted from direct MCMC.

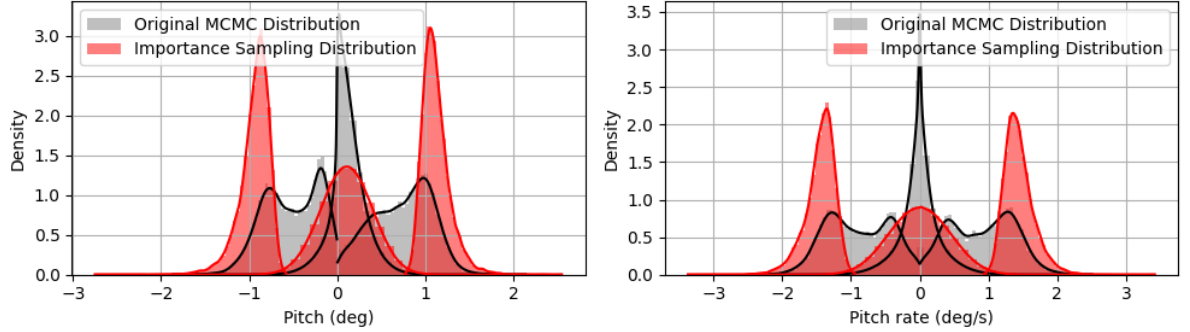


Figure 12: Probability distribution of pitch averaging conditioned to $\xi_{lo}^{\alpha(1)}, \dots, \xi_{lo}^{\alpha(5)}$ ($\epsilon = 0$) vs unconditioned.

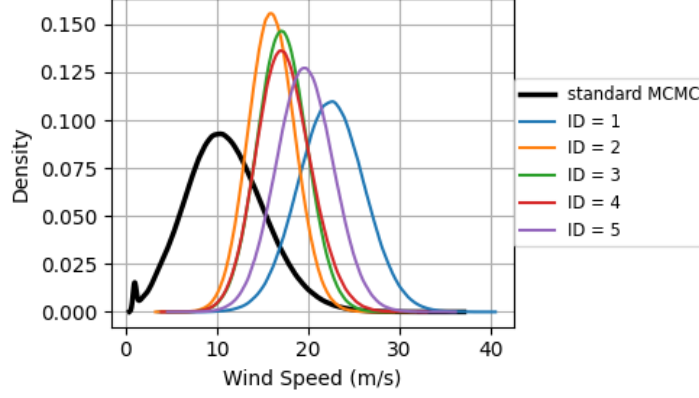


Figure 13: PDFs of wind signal biased by important sampling for selected configurations with $\epsilon = 0$

Of all the anomalous configurations, sample # 2 demonstrates relatively poor sampling performance. The probability of generating the defined rare events is half that of the other samples.

After obtaining initial insights from the experiment with $\epsilon = 0$, we performed importance sampling for each selected configuration using $\epsilon \in \{\pi/8, \pi/6, \pi/4, \pi/2, \pi\}$. Figure 14 illustrates the performance of each selected ϵ for each configuration. Throughout the sampling process, the highest expectation of generating anomaly pitch events reaches 0.1 in sample 5, where $\epsilon = \pi/8$. When ϵ increases to π , the importance sampling shows similar performance to standard MCMC simulations, with an expectation around 0.01. Although sample # 2 demonstrates relatively poor importance sampling performance, the trend remains consistent across different ϵ values.

Figure 15 presents the PDFs of the wind signal for each value of ϵ , averaged across all configurations. This figure demonstrates the impact of different ϵ values on the wind speed distribution and compares these results with the standard MCMC method. When $\epsilon = \pi$, the PDF closely matches that of the standard MCMC, which is consistent with the sampling performance where the expected value is approximately 0.01. As ϵ decreases, the wind speed PDFs shift towards higher wind speeds and the distribution becomes more concentrated.

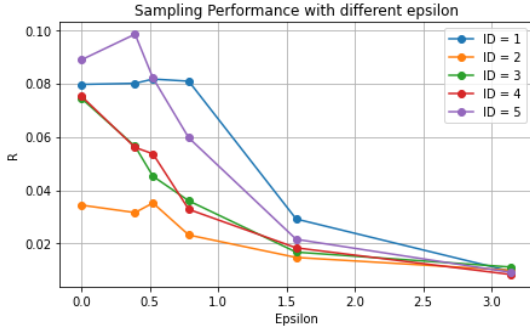


Figure 14: Important sampling performance with different ϵ

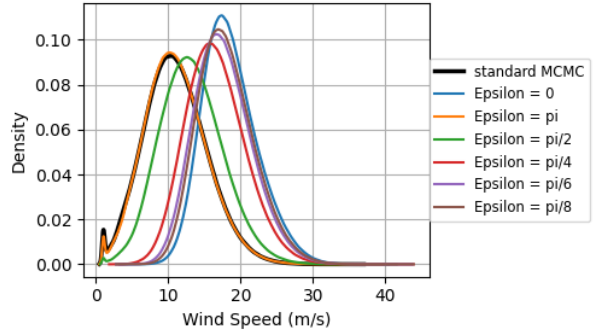


Figure 15: PDFs of wind signals averaged all configurations biased by important sampling for different values of ϵ

3.2.2 Reference Sample for Extreme Surge Events

The surge instability described in [5], associated with active pitch control, is examined under still water conditions with a constant rated wind speed of 11.4 m/s. In this scenario, the surge oscillates between -1m and 8m . This instability can become more severe under stochastic conditions.

Figure 16 shows the PDFs of the surge and extreme values of 10,000 samples from standard MCMC simulations. The overall standard deviation of surge displacement is 1.387m . The distribution of extreme values under stochastic conditions reveals that surge instability can range from -8 m to 12 m , indicating significantly stronger fluctuations than those characterized in [5].

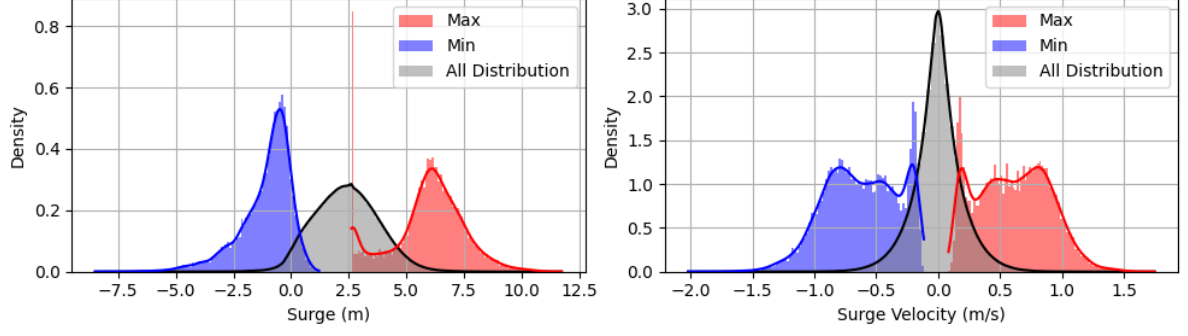


Figure 16: Surge and surge velocity distribution

Figure 17, 18 illustrates examples of extreme surge events derived from the standard MCMC simulation. Figure 17 shows the surge fluctuating from -3m to over 10m . The platform initially moves to its maximum offset of over 10m in the positive direction (aligned with the wind speed) then swinging back and overshooting to a minimum value of approximately -3m . Figure 18 demonstrates the platform first reaching a minimum of -7m first, then swinging back to a maximum of 8m . This opposite direction of initial movement suggests two types of events, each likely caused by different factors.

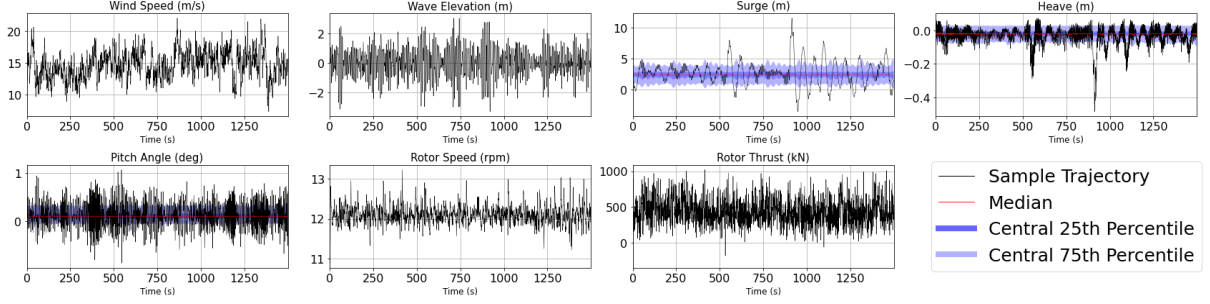


Figure 17: Extreme Surge fluctuations from 500s - 1500s.

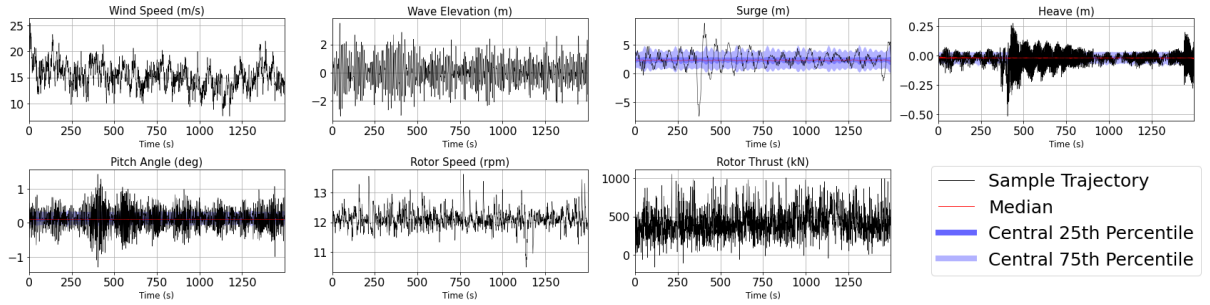


Figure 18: Extreme Surge fluctuations from 300s - 800s.

We focus on the type of events shown in Figure 17. The event is indicated when the surge exceeds a certain threshold θ . Thus we define the characterize function $\chi_\zeta(\cdot)$ as follows:

$$\chi_\zeta(\xi^\zeta, \theta) = \begin{cases} 0, & \text{if } \forall t \in [0, T], \zeta(t) < \theta \\ 1, & \text{if } \exists t \in [0, T] \text{ s.t. } \zeta(t) \geq \theta. \end{cases} \quad (27)$$

Where $\zeta(t)$ is the surge state component in Eq. (1).

To gain insights into performing IS, we first analyzed the events sampled using standard MCMC. We calculated the probability of a sample with surge fluctuations exceeding 8m , 9m , and 10m . Table 3 presents the results. In the this subsection, we demonstrate and discuss the performance of the important sampling method for this type of event.

$P(\text{surge} > 8m)$	$P(\text{surge} > 9m)$	$P(\text{surge} > 10m)$
0.0746	0.0210	0.0053

Table 3: Probability of a sample with surge exceeding 8m, 9m, and 10m.

We repeated the IS procedure previously applied to pitch events. We selected the first configuration and extracted the large-scale wind component $\xi_{lo}^{\zeta(1)}$ from the sample shown in Figure 17, and initiated IS at $\epsilon = 0$ with a convergence test. The results are presented in Table 4, and we keep our choice for sampling size as 2,500.

Sampling Size	$\mathbb{E}[\chi_{\zeta}(\xi_{lo}^{\zeta(1)}, 8m)]$	$P(\text{surge} > 9m)$	$P(\text{surge} > 10m)$
1,500	0.199	0.076	0.018
2,500	0.199	0.0676	0.0176
5,000	0.206	0.0668	0.0180
10,000	0.2	0.0671	0.0173
20,000	0.2	0.0661	0.0185

Table 4: Probability of a sample with surge exceeding 8m, 9m, and 10m at different sampling sizes.

Comparing the probabilities in Table 4 and 3, we observe a significant increase in the expectation of capturing samples with extreme surge events through IS. Specifically, when the threshold is set at 8 meters, IS increases the probability of a surge exceeding this threshold by a factor of 2.68. For a surge exceeding 9 meters, the probability is increased by 3.14 times, and for a surge exceeding 10 meters, the probability rises by 3.4 times. As the threshold becomes more extreme, the amplification effect of IS becomes more pronounced.

Subsequently, we selected 4 more configurations $\xi_{lo}^{\zeta(2)}, \dots, \xi_{lo}^{\zeta(5)}$ by choosing samples corresponding to the same type of extreme events depicted in Figure 17, conducting sampling with $\epsilon \in \{0, \pi/8, \pi/6, \pi/4, \pi/2, \pi\}$ for each configuration.

We start by presenting the results for all configurations with $\epsilon = 0$. Figure 19 compares the PDFs of surge and its extreme value from IS averaging all configurations and standard MCMC. Table 5 displays the expectation of a sample with surge exceeding the 8m, 9m, and 10m thresholds for each configuration. Across all configurations, there is an increased likelihood of generating these extreme surge events. Notably, Configuration 3 stands out with significantly higher probabilities for generating extreme surge events compared to the others. Specifically, Configuration 3 shows a 4.96% chance of surges exceeding 10m which is almost 10 times more effective than using standard MCMC.

Configuration ID	$P(\text{surge} > 8m)$	$P(\text{surge} > 9m)$	$P(\text{surge} > 10m)$
1	0.199	0.0676	0.0176
2	0.174	0.0628	0.0156
3	0.290	0.124	0.0496
4	0.233	0.0832	0.0208
5	0.156	0.0472	0.0096

Table 5: Probability of a sample with surge exceeding 8m, 9m, and 10m for selected configurations.

We also compare the PDFs of wind signals biased by each configuration with those obtained using standard MCMC in Figure 20. Configurations tend to exhibit a greater bias towards higher and broader wind speed distributions demonstrate a better performance in extreme event sampling. Configuration 3, in particular, shows a significant bias, with its distribution shifted the furthest towards larger wind speeds among all the configurations analyzed resulted the best extreme surge events sampling performance.

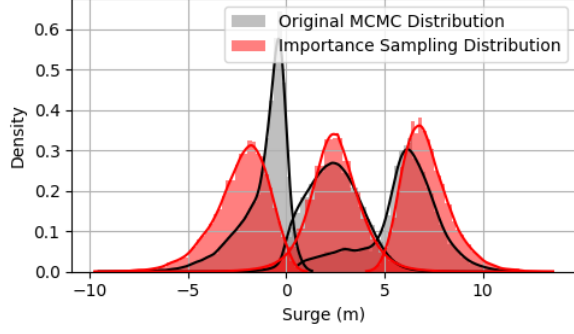


Figure 19: Probability distribution of surge conditioned to $\xi_{lo}^{\zeta(1-5)}$ ($\epsilon = 0$) vs unconditioned.

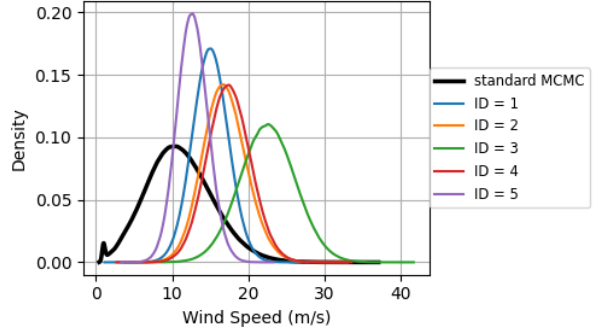


Figure 20: PDFs of wind signals biased by important sampling for selected configurations with $\epsilon = 0$

The role of the parameter ϵ in influencing the probability of extreme surge events is clearly illustrated in Figure 21. The three subplots represent the probability of extreme surge events exceeding thresholds of 8m, 9m, and 10m across five different configurations. The results demonstrate that, for most configurations, the maximum expectation of extreme surge events occurs when $\epsilon = 0$, indicating that the baseline scenario is the most prone to such events. However, a notable exception to this trend is Configuration 2, where the maximum expectation of extreme surge events occurs $\epsilon = \pi/6$.

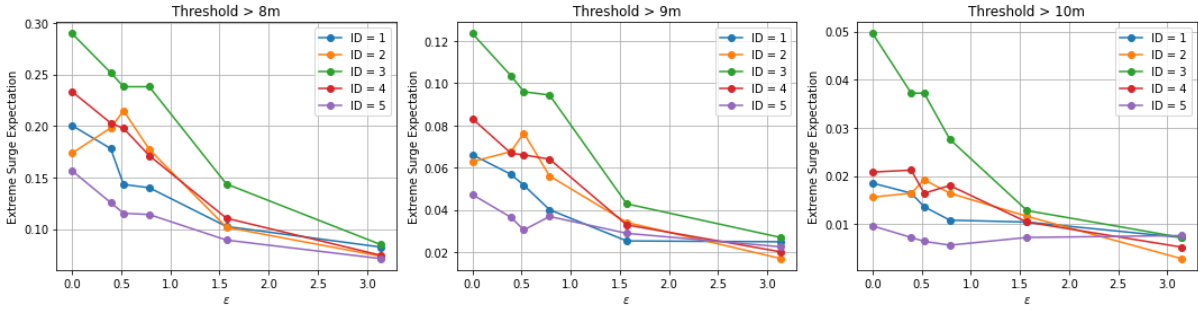


Figure 21: The expectation to sample extreme surge events with different ϵ at threshold 8m, 9m, and 10m

3.3 Multi-Sample IS Implementation

We follow the formulation in Eq. (22) extending the IS approach to incorporate multiple configurations derived from brute-force MCMC. For each configuration, a large-scale wind component is randomly selected, and IS is performed by biasing the selected configuration while conditioning the small-scale wind and wave components accordingly.

We provide the implementation example for the extreme surge events here. It can also applied to other features. We choose 15 configurations with the largest surge value from 10,000 MCMC samples, and let the large-scale wind component $\xi_{lo}^{\zeta(1-15)}$ for those 15 samples serve as an empirical probe function for IS. Figure 22 illustrates the exponential decline in the probability of encountering a sample with extreme surge events as the threshold increases. The three red markers correspond to the results from the previous section, where the values were obtained by averaging the columns of Table 5. Notably, these red dots align with the new $N = 15$ experiment at $\epsilon = 0$. Figure 23 shows the wind signal distribution biased by the selected 15 configurations at different values of ϵ .

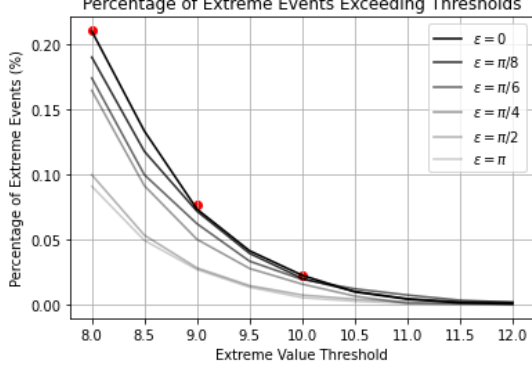


Figure 22: The average percentage of samples with the surge exceeding thresholds for 15 configurations at different ϵ .

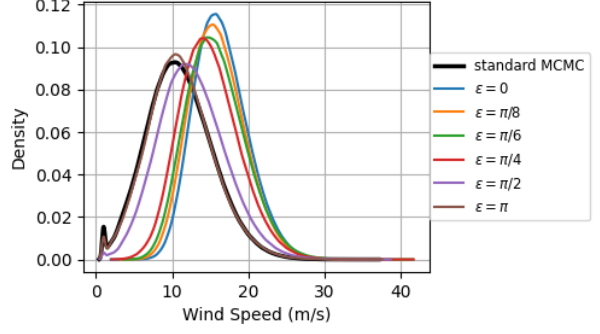


Figure 23: PDFs of wind signals biased by 15 configurations at different value of ϵ

4 Non-parametric Adaptive Importance Sampling

In this section, we present an adaptive importance sampling (AIS) by utilizing the non-parametric Cross-Entropy (CE) method. In Section 3, we introduced and implemented the empirical IS which defines the proposal probe function q from the brute-force MCMC method.

4.1 Cross-Entropy Method Formulation

Recall the IS estimated to calculate the probability of a rare event indicated by $\chi(\cdot)$ using Eq. (19). Given N configurations drawn from brute-force MCMC method $\{\xi_{lo,i}\}_{i=1}^N$ drawn from $q(\xi_{lo})$, the unbiased estimator of R is:

$$\hat{R} = \frac{1}{N} \sum_{i=1}^N \chi(\cdot) w_i, \quad (28)$$

where the importance weights w_i are computed as:

$$w_i = \frac{p_{\text{ex}(lo)}(\xi_{lo,i})}{q(\xi_{lo,i})}. \quad (29)$$

where $p_{\text{ex}(lo)}$ is the true probability density function (PDF) of the large-scale component ξ_{lo} . We employ IS by introducing a proposal distribution $q(\xi_{lo})$.

The optimal importance sampling distribution $q^*(\xi_{lo})$ minimizes the variance of the estimator and is given by:

$$q^*(\xi_{lo}) = \frac{\chi(\cdot) p_{\text{true}}(\xi_{lo})}{R}. \quad (30)$$

However, $q^*(\xi_{lo})$ depends on the unknown R and is generally intractable. Therefore, we seek to approximate $q^*(\xi_{lo})$ by updating $q_k(\xi_{lo})$ iteratively.

4.2 Cross-Entropy Method Implementation

4.2.1 AIS Generating Extreme Surge Events

4.2.2 AIS Analysis Mooring System Stress

5 Conclusion

These approaches, often referred to as 'instantons' in statistical mechanics and mathematics, aim to identify the most probable wind and wave patterns that could push FOWTs beyond safe operational limits. The discovery of such instantons, followed by the development of adaptive importance sampling techniques inspired by similar studies in other application domains [? ? ? ?], represents a natural progression of our analysis. We anticipate that once adaptive importance sampling techniques are developed for a reduced model (like the Betti model used in this study), and the importance sampling probe

function along with significant wind and wave events causing anomalies in pitch, heave, and surge are identified and explained, it will be straightforward to assess the significance of these extreme events for high-resolution models, such as [4].

Moreover, it is essential to integrate these emergent rare event methodologies with existing FOWT reliability literature [? ?]. We plan to incorporate comprehensive reliability constraints, such as construction integrity, wear and tear, and maintenance costs, into our instanton-based adaptive sampling methods.

Finally, integrating sensitivity analysis into rare event reliability studies of FOWT is a crucial future direction. We aim to develop methodologies for real-time identification and mitigation of hazardous patterns, incorporating robustness against the fine details of wind and wave patterns. We anticipate leveraging established uncertainty identification techniques, such as polynomial chaos [? ?], and also modern AI techniques, such as differential programming [?] and generative models, to advance the sensitivity analysis in FOWT research [? ?].

References

- [1] Y. Liu and M. Chertkov, “Anomalous Response of Floating Offshore Wind Turbine to Wind and Waves,” Feb. 2024. [Online]. Available: <https://wes.copernicus.org/preprints/wes-2024-14/>
- [2] American Clean Power Association, “Wind power facts,” 2023, accessed: 2023-07-26. [Online]. Available: <https://cleanpower.org/facts/wind-power/>
- [3] G. Betti, M. Farina, G. A. Guagliardi, A. Marzorati, and R. Scattolini, “Development of a Control-Oriented Model of Floating Wind Turbines,” *IEEE Transactions on Control Systems Technology*, vol. 22, no. 1, pp. 69–82, Jan. 2014. [Online]. Available: <http://ieeexplore.ieee.org/document/6451223/>
- [4] J. Jonkman, S. Butterfield, W. Musial, and G. Scott, “Definition of a 5-mw reference wind turbine for offshore system development,” 2 2009. [Online]. Available: <https://www.osti.gov/biblio/947422>
- [5] D. Matha, “Model development and loads analysis of an offshore wind turbine on a tension leg platform with a comparison to other floating turbine concepts: April 2009,” 2 2010. [Online]. Available: <https://www.osti.gov/biblio/973961>
- [6] M. Karimi, M. Hall, B. Buckham, and C. Crawford, “A multi-objective design optimization approach for floating offshore wind turbine support structures,” *Journal of Ocean Engineering and Marine Energy*, vol. 3, pp. 1–19, 02 2017.
- [7] I. V. der Hoven, “Power spectrum of horizontal wind speed in the frequency range from 0.0007 to 900 cycles per hour,” *Journal of Atmospheric Sciences*, vol. 14, no. 2, pp. 160 – 164, 1957. [Online]. Available: https://journals.ametsoc.org/view/journals/atsc/14/2/1520-0469_1957_014_0160_psohws_2_0_co_2.xml
- [8] C. Nichita, D. Luca, B. Dakyo, and E. Ceanga, “Large band simulation of the wind speed for real time wind turbine simulators,” *IEEE Transactions on Energy Conversion*, vol. 17, no. 4, pp. 523–529, 2002.
- [9] G. Komen and K. Hasselmann, “On the existence of a fully developed wind-sea spectrum,” *Journal of Physical Oceanography - J PHYS OCEANOGR*, vol. 14, pp. 1271–1285, 08 1984.
- [10] A. B. Owen, “Change of Variables in Monte Carlo Integration.” [Online]. Available: <https://artowen.su.domains/mc/Ch-var-is.pdf>
- [11] B. B. Sorensen, A. Charalampopoulos, S. Zhang, B. Harrop, R. Leung, and T. Sapsis, “A non-intrusive machine learning framework for debiasing long-time coarse resolution climate simulations and quantifying rare events statistics,” Feb. 2024, arXiv:2402.18484 [physics]. [Online]. Available: <http://arxiv.org/abs/2402.18484>